A magnetic mesoporous chitosan based core-shells biopolymer for anionic dye adsorption: Kinetic and isothermal study and application of ANN

Bahareh Tanhaei,[1,2] Ali Ayati,[1,2] Manu Lahtinen,[3] Behrooz Mahmoodzadeh Vaziri,[4] Mika Sillanpää[1]

[1]Laboratory of Green Chemistry, LUT School of Engineering Science, Lappeenranta University of Technology, Sammonkatu 12, FI-50130 Mikkeli, Finland
[2]Department of Chemical Engineering, Quchan University of Advanced Technology, Quchan, Iran
[3]Department of Chemistry, Laboratories of Inorganic and Analytical Chemistry, University of Jyväskylä, JY, FI-40014, Finland
[4]Department of Chemical Engineering, Quchan Branch, Islamic Azad University, Quchan, Iran
Correspondence to: B. Tanhaei (E-mail: b.tanhaei@yahoo.com or b.tanhaei@qiet.ac.ir)

ABSTRACT: In this study, Chitosan/Al_2O_3/Fe_3O_4 core-shell composite microsphere (CAMF) was used as an effective sorbent with high adsorption capacity for the removal of anionic azo dye model from aqueous solution. The obtained composite was characterized by XRD, SEM, EDX, and BET analysis. The results showed the high methyl orange (MO) adsorption in a wide pH range of 4–10 and the optimum adsorbent dosage was obtained 0.6 g L^{-1}. It is indicated that the equilibrium data followed the Langmuir isotherm model and the adsorption kinetic was well fitted with pseudo-second-order kinetic model. Also, the adsorption kinetic was controlled by the film diffusion and intra-particle diffusion, simultaneously. It is revealed that by increasing the particle size from <0.1 μm to ~0.4 μm, the adsorption capacity did not change, significantly. The adsorption capacity of MO on CAMF was predicted by multilayer perceptron (MLP) neural network at different initial MO concentration, in which the predictions of MLP model had very good agreement with experimental data. © 2016 Wiley Periodicals, Inc. J. Appl. Polym. Sci. **2016**, *133*, 43466.

INTRODUCTION

In last years, adsorbents containing natural polymers and biopolymers have received great attention for the removal of organic and inorganic water contaminants.[1–4] Chitosan as one of the most abundant harmless biopolymers in nature, has been widely used in food, pharmaceutical and medical processes and agricultural drugs.[5,6] Its high contents of amino and hydroxyl functional groups make it a low cost adsorbent with high adsorption potential for various aquatic pollutants in the water pollutants treatment.[5,7,8]

In the adsorption processes, the separation of chitosan-based adsorbents from treated solution is commonly carrying out using traditional separation methods, such as filtration and sedimentation, which may result in blocking the filters or loss of adsorbent and make secondary pollutions.[9] Magnetic separation technology by combination of chitosan and magnetic compounds is an efficient strategy to overcome this drawback. These techniques are convenient, rapid, low cost and amenable to automation methods.[10] In this regard, magnetic core–chitosan shell materials are widely employed for the wastewater treatment and iron oxide is

the most commonly used magnetic core due to its strong superparamagnetic behavior, low toxicity and ease of synthesis.[11,12]

The adsorbent particles size is expected to play an important role in adsorption processes due to its effect on the relative abundance of the different crystalline faces and their associated binding sites.[13,14] It has been investigated to understand the adsorption phenomena and producing and selecting an appropriate size for a target pollutant.[15,16] In our previous study, we designed a novel Chitosan/Al_2O_3/Fe_3O_4 nanocomposite (CANF), as a superadsorbent for methyl orange (MO) removal.[17] In which, the Fe_3O_4 nanoparticles were used as magnetic cores which coated with alumina as a shell to improve their chemical stability and prevent their oxidation, especially in acidic conditions.[18,19] In this study, we prepared this composite in micro size (CAMF), in order to study its adsorption performance for the removal of MO as an anionic azo dye. So, the iron oxide magnetic microspheres were prepared by solvothermal method and coated with a uniform shell of alumina. The adsorption kinetic and isotherms of designed magnetic CAMF were studied, comprehensively and also, the adsorption performance was compared with the nanostructures (CANF).

Applying artificial neural networks (ANNs) for such systems is very useful, because these networks are capable to do nonlinear mapping and process modeling without necessity for detailed theoretical knowledge.[20,21] The removal process of MO using CAMF adsorbent is a nonlinear system with interaction between the variables and unknowns. So, in this work, a multilayer perceptron (MLP) neural network model was used as a sufficient tool, for predicting of MO adsorption capacity onto CAMF over a wide range of contact time.

EXPERIMENTAL

Chemicals and Instruments

Chitosan and Acetic acid (100%) were purchased from Acros Organics and VWR Companies, respectively. Glutaraldehyde solution (25%), aluminium isopropoxide ($\geq$98%) and Methyl Orange were all supplied by Sigma-Aldrich Co. and the sodium acetate (NaAc, $\geq$99%), ethylene glycol, polyethylene glycol 4000 and iron (III) chloride hexahydrate were obtained from Merck Company. Also, absolute methanol was supplied from Altia Company.

The powder X-ray diffraction (XRD) analysis was applied to study the crystalanity, composition, content and average particle size of CAMF particles and it was done using PANalytical X'Pert PRO alpha 1 diffractometer. The primary beam Johansson monochromator generated the pure Cu K$_{\alpha 1}$ radiation (1.5406 Å; 45kV, 30mA) and each sample was prepared onto a silicon-made (producing zero-background signal) sample holder using petrolatum jelly as an adhesive. The records were collected by X'Celerator detector using continuous scanning mode in 2θ range of 10–92° with a step size of 0.017° and counting time of 140 s per step (overall time of $\sim$ 90 min). The ICDD PDF-4+ powder diffraction database,[22] implemented with X'pert HighScore Plus v. 2.2d program, was used for the qualitative phase analysis of the XRD patterns, as well as for calculating the average crystal size of the identified phases using Scherrer equation ($K = 0.90$).

The Hitachi S-4800 Ultra-High Resolution Scanning Electron Microscope was used for analysis of morphology and size of reluctant products. It was equipped with EDX analysis for determination of elemental analysis. The EDX model and its detector type were S4800 (I) and 7747/17-ME, respectively.

Specific surface area and pore size distributions were measured using a Gemini V. (Micromeritics, USA) through nitrogen adsorption at 77 K in the range of relative pressure (P/P_0) of $10^{-6}-1$. The pore volume distribution as a function of pore size was calculated on the basis of the Barret, Joyner and Halenda (BJH) method. Finally, A JASCO V-670 spectrophotometer (Japan) was employed to measure the concentration of azo dye MO.

Synthesis of Iron Oxide Microspheres

The iron oxide microspheres were synthesized according to the reported method by Deng et al.[23] In a typical experiments, 1.1 g FeCl$_3$·6H$_2$O was dissolved in 32 mL ethylene glycol to form a clear solution, followed by the addition of 2.88 g NaAc and 0.8 g PEG4000. The mixture was stirred strongly for 40 min and then sealed in a Teflon-lined stainless-steel autoclave with capacity of 40 mL. The autoclave was maintained at 200 °C for 8 h and then allowed to cool down to room temperature.

The black prepared products were washed several times with ethanol and dried at 60 °C for 12 h.

Synthesis of CAMF

For the synthesis of CAMF, we used the reported method in our previous study,[17] in which 100 mg of Fe$_3$O$_4$ microspheres were dispersed in the solution of aluminum isopropoxide in ethanol, firstly. The Al$_2$O$_3$/Fe$_3$O$_4$ core-shell spheres (AMF), were prepared by addition of a mixture of water and ethanol [1:5 (v/v)] to the suspension under vigorous magnetic stirring and washed with ethanol, several times and dried in the oven. After that, the calcined magnetic AMF particles (at 500 °C for 3 h) were dispersed in the chitosan containing acetic acid (2 wt %), followed by addition of glutaraldehyde solution (25 wt %) to form a brown gel. It was dried in oven at 60 °C for 12 h and washed with acetic acid solution (2 wt %) and ultra-pure water to remove unreacted chitosan. Then, the obtained particles were dried again at 50 °C for 12 h.

Adsorption and Desorption Study

Adsorption Process. For the adsorption study in the batch mode, a desired amount of CAMF adsorbent was added to a tube containing 10 mL of 20 ppm MO solution and were placed on the Lab Teamet ST5 CAT shaker. The HCl or NaOH (0.01 M) solutions were applied for adjustment of solutions pH in the range of 3−11. Finally, the particles were filtered with 0.45 μm polypropylene membrane and the solutions were analyzed at $\lambda_{max} = 464$ nm. The adsorption percentage (R) and adsorption capacity at equilibrium and t time (q_e and q_t, mg g^{-1}) were calculated using the following equations:

$$\theta = \frac{C_0 - C_e}{C_0} \times 100 \qquad (1)$$

$$q_e = \frac{C_0 - C_e}{m} V, \ q_t = \frac{C_0 - C_t}{m} V \qquad (2)$$

where C_0, C_e, and C_t (mg L^{-1}) are the MO concentrations at initial, equilibrium and t time, respectively, V (L) is the solution volume and m (g) is the adsorbent mass.

To investigate the isotherms, solutions were equilibrated in an IKA KS 4000i Control shaker in a control box to maintain and fix the temperature condition. These experiments were carried out in different temperatures (25, 35, and 45 °C) with varied initial MO concentrations (5−800 mg L^{-1}). Furthermore, the kinetic experiments were done at three different initial MO concentrations (10, 20, and 40 mg L^{-1}) at the equivalent pH value.

Desorption and Regeneration Process. For desorption study, 4 mg of dry adsorbent was added to 10 mL of MO solution (20 ppm) and left for 24 h on the shaker at room temperature. The saturated MO-loaded adsorbent was magnetically collected and washed with distilled water to remove the unadsorbed traces of MO. Next, the adsorbent was agitated with 10 mL of 0.05 M HNO$_3$ or 0.1M HCl for 24 h, followed by adsorbent separation. The collected adsorbent was washed with water for several times to reuse and remove excessive acidity/alkalinity, and dried at 60 °C for 12 h. To test the reusability of the adsorbent, described adsorption–desorption cycle was repeated several times using the same adsorbent.

Kinetic Models. The experimental data were described by the widely used pseudo-first order and pseudo-second order models,[17] Bangham's model equation,[24] and Weber and Morris,[25] which

were applied to study the rate of the adsorption process and examine the possible adsorption mechanisms of MO. The linear forms of pseudo-first-order and pseudo-second-order model equations can be expressed by eqs. (3) and (4), respectively[17]:

$$\ln\left(q_e - q_t\right) = \ln q_e - k_1 t \tag{3}$$

$$\frac{t}{q_t} = \frac{1}{k_2 q_e^2} + \frac{t}{q_e} \tag{4}$$

where q_e (mg g^{-1}) is the adsorption capacity of CAMF in equilibrium; k_1 (min^{-1}) and k_2 (g mg^{-1} min^{-1}) are the rate constants of the pseudo-first-order and pseudo-second-order models, respectively.

Bangham's model equation is generally expressed as equation[24]:

$$\log\log\left[\frac{C_i}{C_i - mq_t}\right] = \log\left[\frac{k_0 m}{2.303 V}\right] + \alpha\log t \tag{5}$$

where V is the solution volume, m is the weight of adsorbent used per liter of solution (g L^{-1}), (mL), C_i is the initial concentration of the adsorbate in the solution (mg L^{-1}) and α (<1), and k_0 are constants.

Also, an intra-particle diffusion model which was proposed by Weber and Morris,[25] was used to investigate diffusion mechanism between the MO molecule, CAMF, and the amount adsorbed. This model is given by the following equation[25]:

$$q_t = k_i t^{1/2} \tag{6}$$

where, C is the value of intercept and k_i (mg g^{-1} min$^{1/2}$) is the intra-particle diffusion rate constant.

MLP Network Structure

ANN learns the relations between the input and output variables from a training data set, constructs a model to fit the data samples and applies the model to predict the outputs of new input data. ANNs have been extensively used in many fields of chemical engineering, such as process modeling, optimization, and control.[20,21]

In this study, a multilayer perceptron (MLP) neural network model was developed for predicting the adsorption capacity of MO onto CAMF surface. The MLP network, as one of the powerful types of feed-forward ANNs, is a good candidate for modeling of processes due to its simple structure and ease of implementation. MLP offers a continuous approximation of a multivariable function, that is not analytically obtainable, but that is properly described by experimental data. It is a widely used network type which is usually applied to all kinds of industrial and also research modeling problems.[26]

The MLP network was trained by back-propagation algorithm. It is based on simple projection procedure which was mostly made by "sigmoid activation (transferring) function" as one of the best global activation function that establish least values of error.

In this study, time and initial concentration of MO were considered as input variables and adsorption capacity was output variable. Consequently, the applied neural network was a Multi-Input Single-Output (MISO) system. The applied MLP network in this study consists of three layers: (a) a transparent input
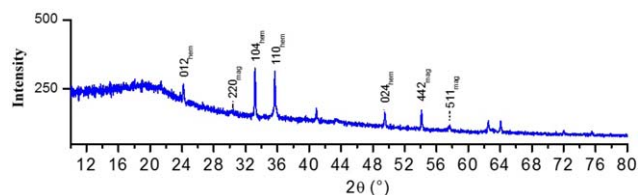

Figure 1. The XRD patterns of prepared CAMF (hem: Fe$_2$O$_3$ and mag: Fe$_3$O$_4$). [Color figure can be viewed in the online issue, which is available at wileyonlinelibrary.com.]

layer which is only used to connect the network to its environment, (b) a hidden layer with sufficient number of neurons applies a nonlinear transformation to the input variables using the sigmoid function, and (c) an output layer contains one node. The number of neurons in hidden layer is fixed by trial and error procedure, so that the error values are minimized. In this regard, eight neurons were selected and applied. It should be noted that the mean squared error (MSE) function had been applied to determine the accuracy of MLP model.

The fifty-four (54) experimental data were used to construct MLP model. The entire experimental data were divided into three parts (training, validation, and test set), randomly. The training set represents a part of data used to train the network namely adjusting the model parameters and the validation set contains of data applied to prevent over-fitting of the network during training. The test set is a part of data for evaluating the network performance on data not used in network training. Training, validating and testing data sets are partitioned to 60%, 20%, and 20% of experimental data, respectively.

On the other hand, if the input variables have not been the same order of magnitude, the training algorithm performs untrustworthy and the forecasting ability of ANN would be decreased. Therefore, the entire set of input variables should be normalized to a specified scale before applying for training or testing processes. It can also help to avoid overflows that might occur due to the severely large or very small weights. The data normalization method was done using following equation:

$$x_{\text{normal}} = \frac{x - x_{\min}}{x_{\max} - x_{\min}} \tag{7}$$

In this way, all of the experimental data were normalized to a scale of zero to one.

RESULTS AND DISCUSSION

Characterization of CAMF

The phase composition and the average crystal sizes of prepared CAMF was investigated by powder X-ray diffraction (see Figure 1). The observed diffraction intensities on CAMF are characteristic for rhombohedral Fe$_2$O$_3$ (hematite) with trace amounts of face-centered cubic Fe$_3$O$_4$ (magnetite), whereas sample Fe$_3$O$_4$ is consisted of Fe$_3$O$_4$ (magnetite) phase only. The broad diffraction hump (from ~10 to 20° 2θ) in the XRD pattern of CAMF corresponds to the amorphous chitosan, as the hump is missing from the chitosan free samples of AMF and iron oxide particles. Crystal size of the assigned iron oxide phases were estimated by Scherrer equation. The crystal size of iron oxide phases for CAMF particles was estimated about 106 nm. By comparing the

samples, it seems that the crystal size is dependent on addition of chitosan as the crystal size of hematite phase is smaller with chitosan but without chitosan crystal size clearly increased from 106, 83, and 76 to 165, 129, and 117 nm for 104, 024, and 311 peak, respectively.

The prepared samples were characterized by SEM analysis and the images are shown in Figure 2(a–d). Figure 2(a) shows the well prepared spherical magnetic Fe_3O_4 nanoparticles with diameter about 0.2−0.5 μm. In the case of AMF core–shell particles, a bulk of Fe_3O_4 spheres which covered by a layer of alumina is appeared. The higher magnification image in Figure 2(b) shows the well-coated particles of iron oxide microspheres. The SEM images of CAMF [see Figure 2(c,d)] represent the final products which exhibit aggregation as a result of magnetic particles embedding inside the cross linked chitosan. The CAMF has a spherical shape and its surface has interspaced structure.

The composition of CAMF was determined by EDX analysis and its spectrum is represented in Figure 2(e). As it can be seen, it confirms the presence of Fe, Al and O and C (due to the carbon tape) in the structure of CAMF with the elemental analysis of 3.2, 4.3, 19.3, and 73.2 wt %, respectively.

In order to study the porous structure characteristics of the prepared CAMF, N_2 adsorption–desorption experiments were carried out which present the type IV adsorbent with an obvious hysteresis loop. The CAMF sample shows a BET surface area of 21.87 m^2 g^{-1}, and the BJH adsorption and desorption cumulative pore volume of 0.024 and 0.028 cm^3 g^{-1}, respectively. Moreover, the BJH adsorption and desorption average pore width were obtained 21.22 and 27.20 Å, respectively.

Surprisingly, however the size of CAMF particles are much more than the CANF, but the BET surface area of CAMF just 0.20 m^2 g^{-1} lower than the CANF one.[17] It might be due the blockage of pore in CANF which decreased its surface area to the CAMF amount. Also, the BJH adsorption and desorption cumulative pore volume of CAMF were 0.003 and 0.006 higher than CANF parameters, however the BJH adsorption and desorption average pore width of CAMF was lower than CANF structure (46.815 and 41.003 Å).[17]

Adsorption Study of CAMF

The MO azo dye was chosen to investigate the adsorption activity of synthesized CAMF. First, the CAMF adsorption capacity was compared with the adsorption capacity of Fe_3O_4 microspheres, chitosan and AMF core shell particles. For this aim, 0.4 g L^{-1} of each adsorbent was added to the MO solution (80 ppm) for 24 h at room temperature. The adsorption capacities were measured 191.63, 38.47, 15.92, and 12.39 mg g^{-1} for CAMF, AMF, chitosan and Fe_3O_4 microspheres, respectively, demonstrating that the adsorption capacity of CAMF is significantly higher than the other adsorbents. Comparing with our previous results[17] revealed that the MO adsorption capacity of Fe_3O_4 microspheres, significantly more than Fe_3O_4 nanoparticles.

The effect of pH on the active sites of adsorbent, makes it an important parameter in the adsorption process.[27] In order to investigate this parameter, the experiments carried out at MO initial concentration of 20 ppm in the presence of 4 mg L^{-1} CAMF and the pH of solutions changed in the range 3-11. Figure 3(a) shows that with increasing of pH from 2 to 4, the removal percentage increased from 35% to 96%. Regardless of increasing pH in the range of 4−10, the removal percentage is almost constant and has a plateau trend, followed by a decrease at pH 11. These results demonstrated that the CAMF shows a high MO adsorption activity (∼96%) in the wide pH range of 4–10 which it might be due to the protonation of amine groups in chitosan prior to adsorption.[28]

At pH = 2, MO molecules were protonated and therefore electrostatic repulsion interaction between protonated MO and positively charged CAMF active sites decreases which would cause to decrease in MO removal percent.[27,29] On the other hand, the decrease of MO adsorption in pH = 11 can be attributed to the competition of the abundant presence of OH^- ions with MO ions for the adsorption sites on the CAMF in basic solution.[27,28] However, at pH of 4−6, due to presence of many active sites in the CAMF, the MO removal percent will be constant. According to the presence of many activated sites in CAMF adsorbent, the presence of OH^- ions in the pH range 6−10 could not affect the MO removal percent. Because of high adsorption activity of CAMF at wide pH range of 4−10, the pH values of MO solutions were unadjusted for further experiments.

In order to find the optimum amount of adsorbent, various amounts of CAMF (0.1–2.6 g L^{-1}) was added to 10 mL of dye solution (20 ppm) and shacked for 24 h and the results are shown in Figure 3(b). The results exhibit that in spite of high removal efficiency, even at low amount of adsorbent, the efficiencies increase by increasing of CAMF dosage in the range of 0.1-0.4 g L^{-1} from 86.6% to 96.4%. For adsorbent dosage more than 0.4 g L^{-1}, it shows a plateau trend by dosage increasing. Actually, in higher adsorbent dosage, the presence of larger surface area and more available adsorption sites cause an increase in the removal efficiency. Beyond the 4 g L^{-1}, the incremental MO removal becomes very low as the surface MO concentration and MO concentration in the solution come to equilibrium with each other.[30] Therefore, increased adsorbent dosage did not enhance the removal percentage.

Furthermore, the adsorption capacity decreases by increasing of adsorbent dosage. As mentioned above, the prepared adsorbent have a plethora of active sites and MO removal percent is high (86.6%), even at the lowest adsorbent amount (0.1 g L^{-1}). When adsorbent amount increased from 0.1 to 2.6 g L^{-1}, the MO concentration in solution changed from 20 to 2.6 and 0.38 mg L^{-1} for lowest and highest values of adsorbent, respectively. Therefore, adsorption capacity would decrease with increasing of adsorbent amount. Based on these results, the optimum dose of adsorbent was determined to be 0.4 g L^{-1} and thereby was used further on in the study. It is interesting that the trends of adsorbent dosage and solution pH effects on the MO adsorption in the CAMF adsorbent are almost similar to CANF.

Isothermal Studies and Thermodynamic Studies

Adsorption isotherms represent the adsorption capacity as a function of adsorbate concentration in the solution at equilibrium
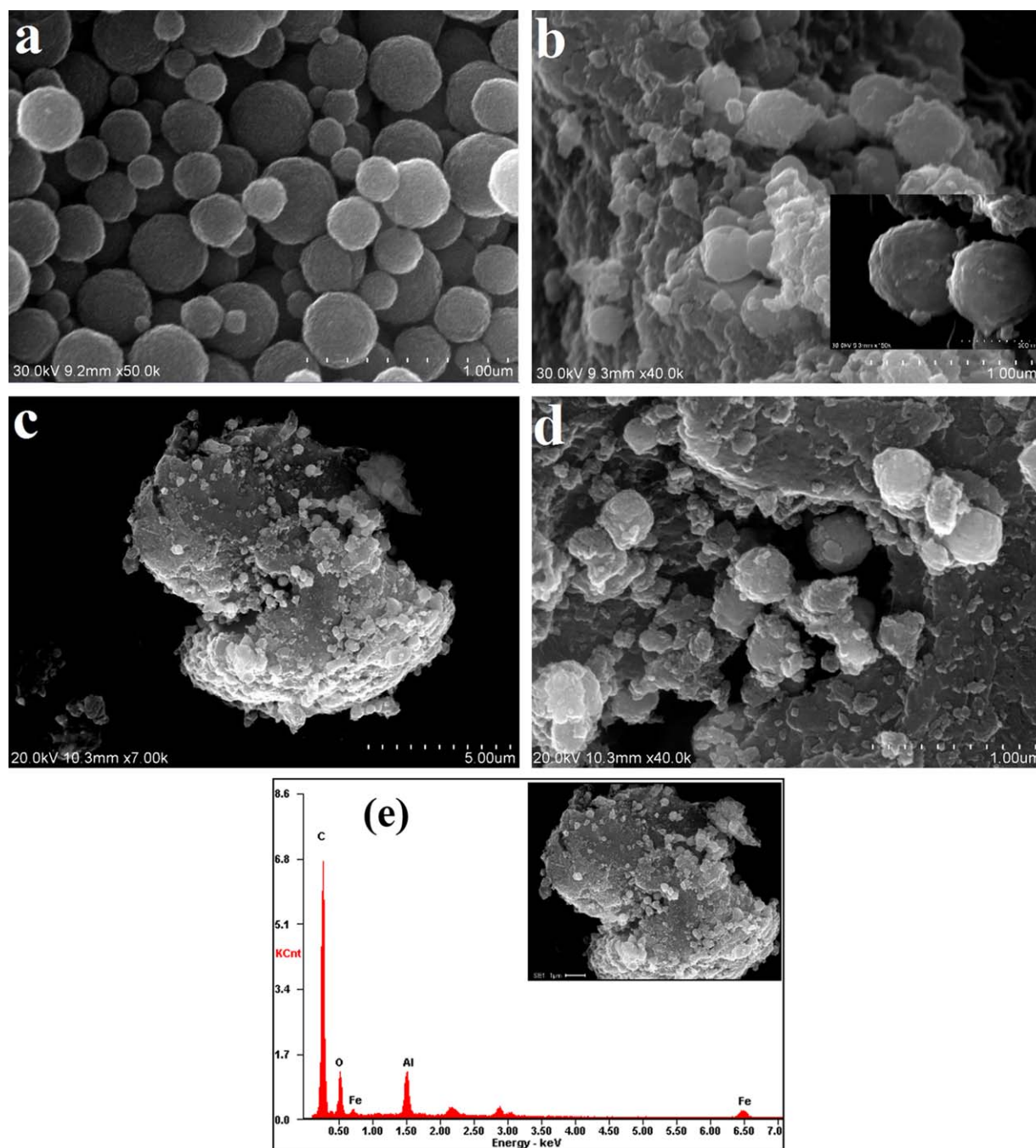
Figure 2. SEM images of (a) Fe_3O_4 microspheres, (b) AMF, (c,d) CAMF, (e) EDX analysis. [Color figure can be viewed in the online issue, which is available at wileyonlinelibrary.com.]

conditions. In this study, the Langmuir and Freundlich isotherm models have been applied to determine the nature of MO adsorption on the CAMF. The linear form of Langmuir isotherm and the well-known logarithmic form of the Freundlich isotherm expressed as eqs. (8) and (9), respectively[1]:

$$\frac{c_e}{q_e} = \frac{1}{K_L q_m} + \frac{c_e}{q_m} \qquad (8)$$

$$\ln(q_e) = \ln(K_F) + \frac{1}{n}\ln(c_e) \qquad (9)$$

where q_m is the maximum monolayer capacity of adsorbent (mg g^{-1}) and K_L, the Langmuir adsorption constant (L mg^{-1}), related to the free energy of adsorption. K_F (L mg^{-1}) and n are Freundlich constants. K_F is the adsorption capacity of the adsorbent and n gives an indication of how favorable the adsorption process. The values of $2 < n < 10$ show suitable, $1 < n < 2$ softly hard, and less than 1 show poor adsorption
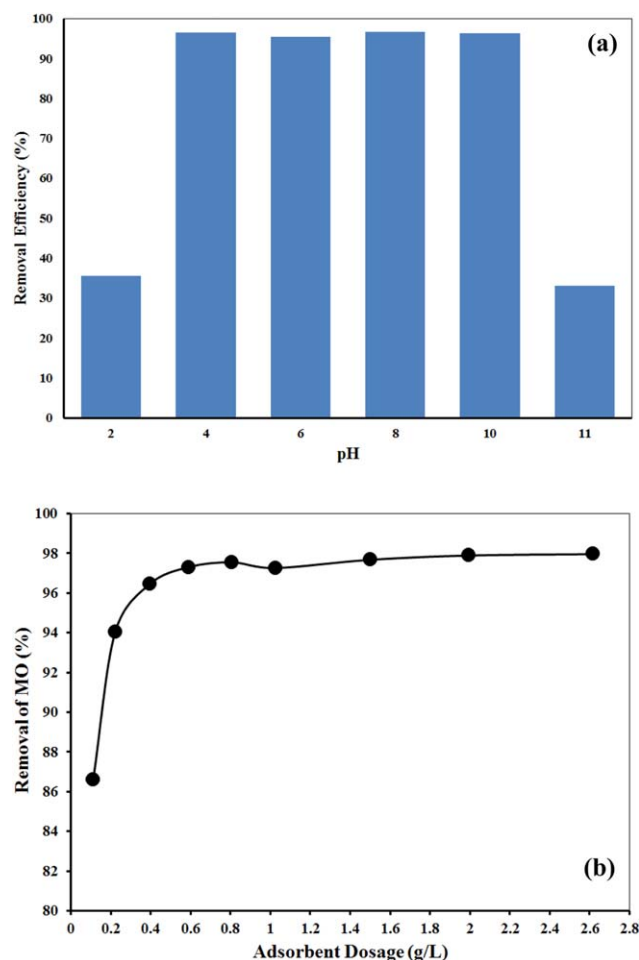
Figure 3. (a) Effect of pH on the MO removal for $C_0 = 20$ mg L^{-1}, $m_{CAMF} = 0.4$ g L^{-1} and $T =$ room temperature (22°C), (b) Effect of adsorbent dose on the removal of MO ($C_0 = 20$ mg L^{-1}). [Color figure can be viewed in the online issue, which is available at wileyonlinelibrary. com.]

enhance sharply at first, and then gently rising to reach a plateau. It means that CAMF could be completely saturated with MO molecules at enough high initial concentrations. With an increase in the initial MO concentrations from 5 to 800 mg L^{-1}, the capacity of adsorbed MO at equilibrium increased from 12.3 to 419 mg g^{-1}, because of the concentration gradient driving force increase accordingly.[32]

Also, as it can be seen in Table I, the adsorption isotherms of MO on the CAMF at different temperatures were fitted nicely using Langmuir isotherm model (evidenced from the correlation coefficients, >0.998). Furthermore, the constant K and q_m, which are derived from the Langmuir and Freundlich theories, decreased with the rise in temperature, thereby confirming a favorable adsorption process at lower temperature. It was shown that the K and q_m constants did not have any trend with temperature for CANF. From Langmuir adsorption isotherms data in Table I, the maximum adsorption capacities of the CAMF for MO were estimated to be 419−388 mg g^{-1} in the range of 298–318 K, respectively.

The regression coefficient ($R^2 > 0.9990$) values, as obtained by linearized isotherms, show better fitting of experimental data towards Langmuir isotherm. Therefore, it suggests that the CAMF adsorbent is structurally homogenous and the adsorption process of MO molecules on CAMF end up in monolayer coverage with uniform adsorption energies.

The separation factor constant (R_L) is a dimensionless parameter that indicates the type of the isotherm to be either favorable ($0 < R_L < 1$), unfavorable ($R_L > 1$), linear ($R_L = 1$) or irreversible ($R_L = 0$).[33] It is defined as eq. (10):

$$R_L = \frac{1}{1 + K_L C_0} \tag{10}$$

where K_L and C_0 are the Langmuir isotherm constant (L mg^{-1}) and initial dye concentration (mg L^{-1}), respectively. The values of the dimensionless constant R_L in this study (Table I) were between 0 and 0.56, implying favorable adsorption of the MO on CAMF.

In order to find out the spontaneously occurring of process, both energy and entropy considerations should be investigated. In this regard, the adsorption studies were carried out at three different temperatures (25, 35, and 45°C) for adsorption of MO (5−800 mg L^{-1}) on the CAMF (0.4 mg L^{-1}) and the results are listed in Table I. The maximum adsorption capacity decreased with an increase in the solution temperature (25−45°C) and it confirms that the adsorption process have an exothermic nature in this study.[34,35] Therefore, the tendency of MO molecules for an

characteristics.[31] The calculated Langmuir and Freundlich adsorption isothermal constants and correlation coefficients are listed in Table I. The experimental data in this adsorption system, can be well fitted using linear Langmuir isotherm and the value of n is between 2 and 10 (Table I) which shows a good adsorption characteristic.

Figure 4 illustrates the effect of MO initial concentrations on the adsorption at 25°C, suggesting that along with an increase in concentrations of MO, the adsorption capacities of CAMF

Table I. Langmuir and Freundlich Adsorption Isothermal Constants, Correlation Coefficients, and the Adsorption Capacities of CAMF for MO

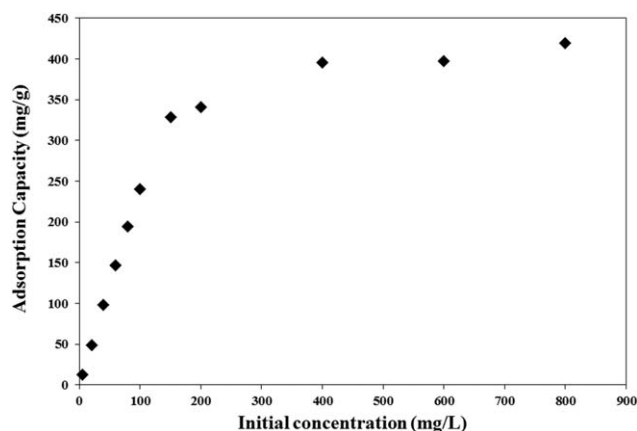| T (°C)	Langmuir model					Freundlich model			ΔG^0 (kJ mol^{-1} K^{-1})	ΔH^0 (kJ mol^{-1} K^{-1})	ΔS^0 (J mol^{-1} K^{-1})
	$q_{m,exp}$ (mg/g)	K_L (L mg^{-1})	$q_{m,cal}$ (mg/g)	R_L	R^2	K_F	n	R^2			
25	419	0.188	416	0.006−0.514	0.9989	85.2	3.2	0.7599	−27.32		
35	405	0.172	400	0.007−0.537	0.9988	81.1	3.1	0.7342	−28.01	−8.39	−63.58
45	388	0.152	384	0.008−0.566	0.9999	65.4	2.9	0.8238	−28.59		

Figure 4. Effect of initial concentrations on the adsorption of MO on CAMF.

adsorption on solid surface would decrease with the temperature increasing due to their escaping from the solid phase to the bulk phase.[35]

The values of thermodynamic parameters such as Gibbs free energy change ($\Delta G°$), standard entropy ($\Delta S°$), and standard enthalpy ($\Delta H°$) were determined using the following Van't Hoff equations[33,36]:

$$\Delta G^0 = -RT \ln K_L \qquad (11)$$

$$\Delta G^0 = \Delta H^0 - T\Delta S^0 \qquad (12)$$

where R (8.314 J mol^{-1} K^{-1}), T (°K), and K_L (L mol^{-1}) are the gas constant, absolute temperature, and Langmuir constant, respectively. The calculated Gibbs free energy changes are listed in the Table I. All the values of ΔG^0 are negative, which indicates the spontaneously adsorption processes. Besides, ΔG^0 decreased in function of the temperature, suggesting that the adsorption at higher temperatures is more beneficial. The calculated standard entropy and standard enthalpy have been shown in the Table I. The negative ΔS^0 corresponds to an irregular decrease of randomness at the MO/CAMF interface of the whole adsorption process. Also, the negative calculated ΔH confirmed an exothermic adsorption in accordance with the decreasing adsorption capacity with an increasing adsorption temperature.[36]

Adsorption Kinetic Study

The effect of contact time on MO adsorption was studied in the solutions containing fixed adsorbent amounts (0.4 g L^{-1}) at different initial concentrations of MO (10, 20, and 40 ppm) and it was observed that the dye uptake increases with the time. At MO concentration of 10, 20, and 40 ppm, 50, 90, and 180 min, respectively, was required to reach 90% adsorption level and about 50%

Table II. Kinetic Parameters for the Adsorption of MO onto CAMF at Different Initial Concentrations by Different Models

Parameters for Pseudo-first order model				
C_0 (mg L^{-1})	$q_{e,exp}$ (mg g^{-1})	$q_{e,cal}$ (mg g^{-1})	k_1	R^2
10	25.6	6.51	0.0116	0.7903
20	48	12.78	0.0109	0.8325
40	98.2	38.16	0.0075	0.8328

Parameters for Pseudo-second order model				
C_0 (mg L^{-1})	$q_{e,exp}$ (mg g^{-1})	$q_{e,cal}$ (mg g^{-1})	k_2	R^2
10	25.6	25.44	0.0173	0.9997
20	48	47.39	0.0077	0.9995
40	98.2	96.15	0.0016	0.9991

Parameters for Intra-particle diffusion model				
C_0 (mg L^{-1})	$k_{i,1}$	$k_{i,2}$	$k_{i,3}$	$k_{i,4}$
10	11.102	0.491	0.1178	0.0087
20	11.612	0.985	0.1363	0.0277
40	32.08	4.23	0.7944	0.2112

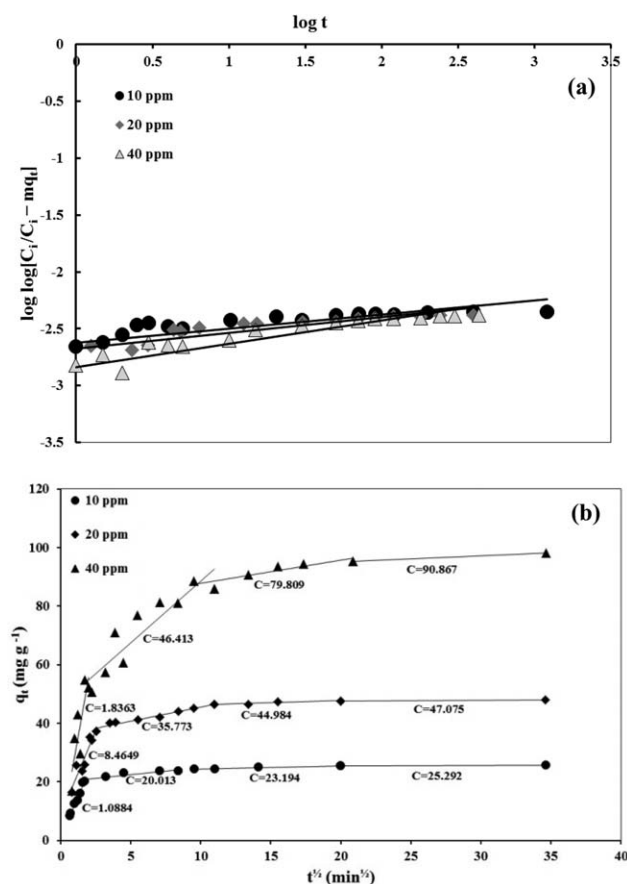| Parameters for Bangham's equation			
C_0 (mg L^{-1})	k_0	α	R^2
10	13.75	0.12	0.7352
20	12.15	0.14	0.7985
40	8.34	0.20	0.8228

Figure 5. (a) The linear plot of Bangham's model, and (b) the intra-particle diffusion kinetic model fit for the adsorption of MO on CAMF.

of the MO was adsorbed in 1, 1.25, and 4 min, respectively. These results confirmed the rapid MO adsorption of CAMF.

On the other hand, the adsorption capacity increased rapidly during the initial adsorption stage and then further increases at a relatively slow adsorption rate, and finally reaches equilibrium after ∼50 min, beyond which there was almost no increase in adsorption capacity. The slow pore diffusion of MO ions into the bulk of CAMF cause to decrease MO adsorption rate.

The adsorption mechanism was studied using four adsorption kinetics models, including pseudo-first-order, pseudo-second-order, Bangham's, and Weber and Morris models. The calculated results are listed in the Table II.

Using the pseudo-fist-order model [eq. (3)], the values of experimental q_e do not confirm the calculated ones and the obtained correlation coefficient (R^2) values are relatively low. It shows that the adsorption process may not correctly be adaptable to the first-order rate equation.

On the other hand, the pseudo-second-order model well fitted with experimental data for the adsorption MO on CAMF. Referring to Table II, the R^2 values for the pseudo-second-order adsorption model have high value (>0.9990) show good agreement between experimental and calculated q_e values at different initial concentrations.
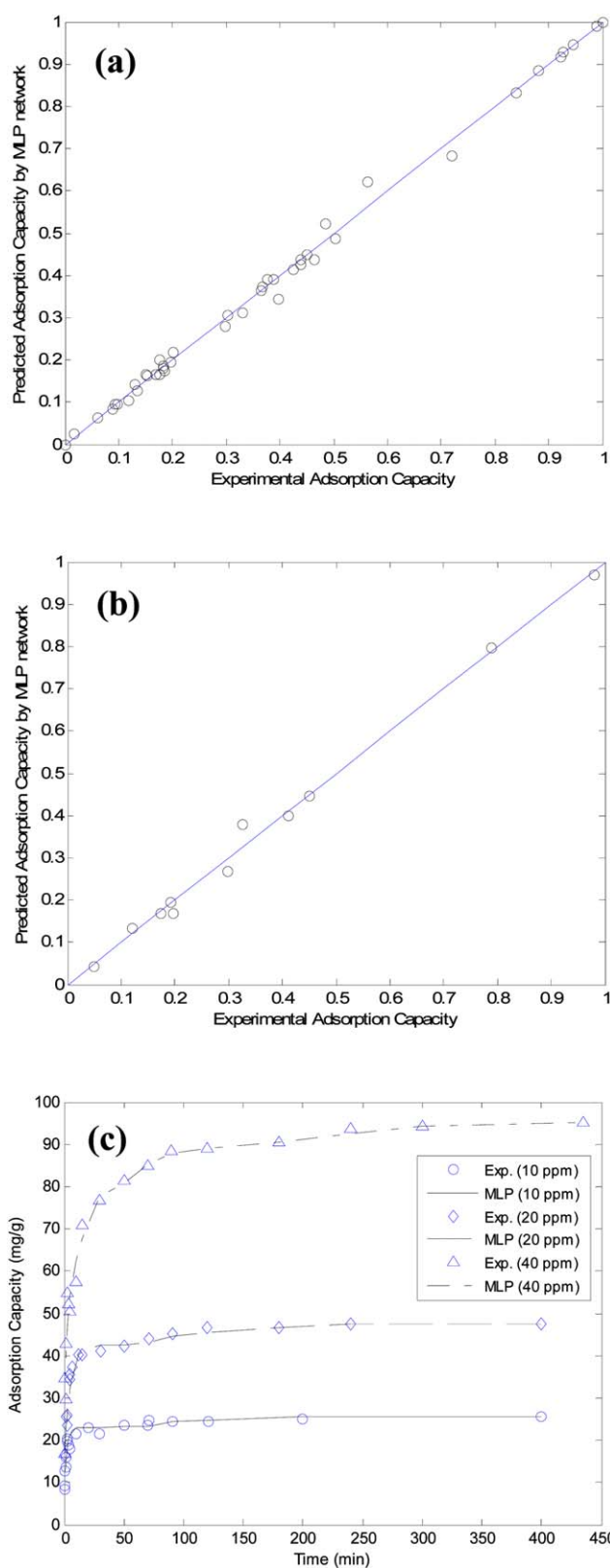

Figure 6. (a) Recall performance of MLP network for prediction of adsorption capacity ($R = 0.998$), (b) Generalization performance of MLP network for prediction of adsorption capacity ($R = 0.997$), and (c) the effect of contact time on the MO adsorption by CAMF along with predictions of MLP model (initial concentration of MO = 10 ppm). [Color figure can be viewed in the online issue, which is available at wileyonlinelibrary.com.]

Table III. Maximum Monolayer Adsorption Capacities (q_m, mg/g) of MO on Different Core-Shell Adsorbents

Adsorbent	Conditions	q_m (mg/g)	References
Maghemite/Chitosan Nanocomposite Films	57°C, 100 rpm, pH = 3	29.41	36
Y-Fe_2O_3/SiO_2/chitosan composite	37°C, 100 rpm	34.29	40
Chitosan/Kaolin/γ-Fe_2O_3 nanocomposites	37°C, 100 rpm, pH = 7	37	41
Preyssler acid/chitosan/Fe3O4	45°C	88.5	42
Fe_3O_4/C/Polyaniline		120.2	43
nano-Fe_3O_4/heulandite/chitosan	pH = 5.5	149.2	44
Cu/Cu_2O	20°C	344.84	45
Chitosan/Al_2O_3/Fe_3O_4 (CANF)	25°C, 100 rpm, pH = 6	416	17
CAMF	25°C, 100 rpm, pH = 6	419	This study

Also, Table II shows that the R^2 values for Bangham's model are < 0.82 which confirming that the experimental data could not satisfactorily fit with this model for removal of MO onto CAMF. Therefore, the film diffusion is not the only rate controlling parameter and it can be confirmed that the film and pores diffusion were important to different extents in the MO removal process.[24] The linear plots of log $[C_i/C_i - mq_t]$ against log t for calculation of Bangham's model parameters have been shown in the Figure 5(a).

The diffusion mechanism was not identified by the pseudo-first-order and pseudo-second-order kinetic models. So, the Weber and Morris model as an intra-particle diffusion model, was studied, as well. Generally, bulk diffusion or the transfer of adsorbate molecules from the bulk of the solution to the adsorbent surface is first step and then film diffusion or the transfer of adsorbate through the boundary layer to the adsorbent surface is the second step. In the third step, intra-particle diffusion or the migration of the adsorbate from the surface to the interior pores of the particle and chemical reaction via ion-exchange or the adsorption of adsorbate at an active site on the surface of adsorbent is the final step.[37]

The plots shown in Figure 5(b) presents multilinearity, indicating that four steps took place in the adsorption. The first sharper portion in the graph completed before 2.5, 6.4, and 10 min for 10, 20, and 40 ppm of MO, respectively, which may be considered as the instantaneous adsorption or diffusion of MO molecules on to the external surface of adsorbent. It can be observed that the plot in this stage do not pass through the origin. So, intra-particle diffusion is not the only rate controlling step. This indicates that some other processes like boundary layer adsorption may also involve in controlling the rate of adsorption.[37] With increasing of MO concentration from 10 ppm to 40 ppm, intensity of line slope increases. In this step, in high MO concentrations, numerous MO molecules interacted with the active sites on the adsorbent and therefore, intensity of adsorption is high. The MO molecules readily enter into the pores of the adsorbents after all of the exterior active points were occupied.[33] The second and third step described the gradual adsorption, wherein the lines did not pass through zero. The intra-particle diffusion was rate-controlling but not just the rate controlling step. In these steps, MO molecules could be adsorbed by the interior surface of pores.[33]

The last step was attributed to the final equilibrium stage, where intra-particle diffusion started to slow down due to the decrease of MO concentration in solution. The thickness of boundary layer was investigated by values of intercept, C, which the boundary layer effect is greater in the larger intercept.[38] As seen in Figure 5(b), the calculated intercept in each step increased with time. Therefore, the boundary layer diffusion effect[37] in moving of MO molecules into the pores of adsorbent can be expected to increase. Based on the result, mechanism of MO adsorption over the surface of CAMF is twisted, because of both intra-particle diffusion, as well as the surface adsorption contributes to the actual adsorption process.

Furthermore, the values of intra-particle diffusion rate constants follow the order of $k_{i,1} > k_{i,2} > k_{i,3} > k_{i,4}$ (Table II). The first rate constants $k_{i,1}$ for adsorption of different MO concentrations on the CAMF are significantly higher than the others. This may be attributed to the existence of fresh exterior surface of adsorbent in the beginning of adsorption process. Moreover, increasing of MO concentration in the solution causes to rapid increasing of k_i. The boundary layer diffusion control may lead to the leaving adsorption mechanism from the intra-particular mechanism. The MO concentration increasing in the solution could prevent the adsorption of MO molecules to the surface and, thus effecting the rate of adsorption.[39]

Application of ANN

The performance of MLP networks strongly depends on the training algorithm to obtain adjustable network parameters, such as synaptic weights and number of neurons. If they have not been sufficiently selected, the MLP network may not have appropriate validity and accuracy. In order to show the model validation, the recall and generalization performances of trained MLP network for prediction of adsorption capacity are presented in Figure 6(a,b).

As it can be seen in Figure 6(a), the recall predictions are in good accordance with almost all training experimental data ($R^2 = 0.998$ and MSE = 101.67), due to the sufficient degrees of freedom of the system. It is worthy of mention that the overfitting phenomenon did not happen in MLP model predictions as shown in Figure 6(b), indicating that the generalization performance provides high acceptable trend for predicting the adsorption capacity ($R^2 = 0.997$ and MSE = 38.23).

The experimental results accompany with predictions of MLP neural network are shown in Figure 6(c). As it can be seen in this figure, the trained MLP network was superiorly able to predict the adsorption capacity versus contact time at different initial MO concentrations. The advantage of applying the well trained MLP network is that adsorption capacity at any contact time can be rapidly predicted without carrying out any experiment.

Desorption and Reusability Studies

From the practical point of view, recovery and separation of adsorbent is important in the industrial applications. So, to check the economic feasibility of the adsorption process, desorption experiments and reusability experiments were performed for the CAMF. According to the previous study,[17] CAMF renewed with $0.1M$ HCl, easily and can be used repeatedly as an efficient adsorbent for practical wastewater treatment. The results of adsorption-desorption cycles showed that the MO adsorption efficiency for CAMF (dose of CAMF= 0.4 mg L^{-1}; initial MO concentration = 60 ppm) still maintained above 99% after 5 operation cycles of repeated regeneration and usage.

Adsorbent Comparison

Also, the maximum adsorption capacity (q_m value) of MO on the CAMF composite and some other core-shell adsorbents was compared and are shown in Table III. It can be seen that q_m value of MO on the CANF is slightly lower than CAMF and changing the particle size did not have significant effect on the adsorption capacity of studied composites. It is found that CAMF composite is suitable and promising adsorbent for the removal of MO from aqueous solutions.

CONCLUSIONS

In this study, we introduced a novel magnetic chitosan/Al$_2$O$_3$/Fe$_3$O$_4$ microsphere composite as an excellent adsorbent for the removal of Methyl Orange azo dye from aqueous solution. The adsorption capacity of CAMF was found 15.33, 12.03, and 5 times of Fe$_3$O$_4$ microspheres, chitosan and AMF particles, respectively. The CAMF showed high adsorption activity at wide pH range of 4−10 and the optimum adsorbent amount was determined 0.6 g L^{-1}. The adsorption kinetics of MO on the CAMF was studied and it was found that the adsorption can be well described by the pseudo-second-order and intra-particle diffusion models. The fitting of experimental data with Weber and Morris model indicated that the adsorption kinetics will be controlled by film diffusion and intra-particle diffusion simultaneously.

In order to cost and time saving, the adsorption capacity of MO on CAMF adsorbent was predicted by well-trained MLP neural network at any contact time. The predictions of MLP model had excellent accordance with experimental results. Moreover, the analysis of equilibrium data showed that the adsorption isotherm was well described by the Langmuir model with high MO adsorption capacity. Furthermore, the thermodynamic parameters showed that the adsorption process was exothermic and higher temperatures are preferred for the process. Our results demonstrated the reusability of CAMF using $0.1M$ HCl by desorption process, in which its adsorption capacities was maintained above 99% after the 5th adsorption–desorption cycle.

REFERENCES

1. Repo, E.; Warchoł, J. K.; Bhatnagar, A.; Mudhooand, A.; Sillanpää, M. Water Res. 2013, 47, 4812.

2. Repo, E.; Warchol, J. K.; Kurniawanand, T. A.; Sillanpää, M. Chem. Eng. J. 2010, 161, 73.

3. Alvesand, N. M.; Mano, J. F. Int. J. Biol. Macromol. 2008, 43, 401.

4. Ngah, W. S. W.; Teongand, L. C.; Hanafiah, M. A. K. M. Carbohydr. Polym. 2011, 83, 1446.

5. Miretzkyand, P.; Cirelli, A. F. J. Fluor. Chem. 2011, 132, 231.

6. Sashiwaand, H.; Aiba, S. Prog. Polym. Sci. 2004, 29, 887.

7. Wu, F. C.; Tsengand, R. L.; Juang, R. S. J. Environ. Manage. 2010, 91, 798.

8. Bhatnagarand, A.; Sillanpää, M. Adv. Colloid Interface Sci. 2009, 152, 26.

9. Reddyand, D. H. K.; Lee, S. M. Adv. Colloid Interface Sci. 2013, 201-202, 68.

10. Donia, A. M.; Atiaand, A. A.; Elwakeel, K. Z. J. Hazard. Mater. 2008, 151, 372.

11. Guptaand, A. K.; Gupta, M. Biomaterials 2005, 26, 3995.

12. Pisanic, T. R.; Blackwell, J. D.; Shubayev, V. I.; Fiñonesand, R. R.; Jin, S. Biomaterials 2007, 28, 2572.

13. Gaboriaudand, F.; Ehrhardt, J. J. Geochim. Cosmochim. Acta. 2003, 67, 967.

14. Han, Y.; Cao, X.; Ouyang, X.; Sohiand, S. P.; Chen, J. Chemosphere 2016, 145, 336.

15. Greenwald, M. J.; Reddingand, A. M.; Cannon, F. S. Water Res. 2015, 68, 784.

16. Matsui, Y.; Nakao, S.; Sakamoto, A.; Taniguchi, T.; Pan, L.; Matsushitaand, T.; Shirasaki, N. Water Res. 2015, 85, 95.

17. Tanhaei, B.; Ayati, A.; Lahtinenand, M.; Sillanpää, M. Chem. Eng. J. 2015, 259, 1.

18. Giakisikliand, G.; Anthemidis, A. N. Anal. Chim. Acta 2013, 789, 1.

19. Lu, A. H.; Salabasand, E. L.; Schüth, F. Angew. Chem. Int. Ed. 2007, 46, 1222.

20. Vaziriand, B. M.; Shahsavand, A. J. Natur. Gas Sci. Eng. 2013, 13, 30.

21. Kashaninejad, M.; Dehghaniand, A. A.; Kashiri, M. J. Food Eng. 2009, 91, 602.

22. Campus Boulevard, Newton Square, Pennsylvania USA, 2013.

23. Deng, H.; Li, X.; Peng, Q.; Wang, X.; Chenand, J.; Li, Y. Angew. Chem. Int. Ed. 2005, 44, 2782.

24. Mezennerand, N. Y.; Bensmaili, A. Chem. Eng. J. 2009, 147, 87.

25. Weberand, W. J.; Morris, J. C. Proceedings of the International Conference on Water Pollution Symposium, Pergamon, 1962, p 231.

26. Pai, P. S.; Mathew, M. T.; Stackand, M. M.; Rocha, L. A. Tribol. Int. 2008, 41, 672.

27. Arshadi, M.; Salimi Vahid, F.; Salvacionand, J. W. L.; Soleymanzadeh, M. App. Surf. Sci. 2013, 280, 726.

28. Huang, R.; Liu, Q.; Huoand, J.; Yang, B. Arab. J. Chem. 2013, to appear.

29. Obeid, L.; Bée, A.; Talbot, D.; Jaafar, S. B.; Dupuis, V.; Abramson, S.; Cabuiland, V.; Welschbillig, M. *J. Colloid Interface Sci.* **2013**, *410*, 52.

30. Naiya, T. K.; Bhattacharyaand, A. K.; Das, S. K. *J. Colloid Interface Sci.* **2009**, *333*, 14.

31. Li, Y.; Sui, K.; Liu, R.; Zhao, X.; Zhang, Y.; Liangand, H.; Xia, Y. *Energy Proc.* **2012**, *16*, 863.

32. Wu, F. C.; Tsengand, R. L.; Juang, R. S. *Water Res.* **2001**, *35*, 613.

33. Ren, Y.; Abbood, H. A.; He, F.; Pengand, H.; Huang, K. *Chem. Eng. J.* **2013**, *226*, 300.

34. Chen, H.; Zhao, J.; Wuand, J.; Dai, G. *J. Hazard. Mater.* **2011**, *192*, 246.

35. Venkatesha, T. G.; Viswanatha, R.; Nayakaand, Y. A.; Chethana, B. K. *Chem. Eng. J.* **2012**, *198-199*, 1.

36. Jiang, R.; Fu, Y. Q.; Zhu, H. Y.; Yaoand, J.; Xiao, L. *J. Appl. Polym. Sci.* **2012**, *125*, E540.

37. Hosseini, S.; Khan, M. A.; Malekbala, M. R.; Cheahand, W.; Choong, T. S. Y. *Chem. Eng. J.* **2011**, *171*, 1124.

38. Dogan, M.; Ozdemirand, Y.; Alkan, M. *Dyes Pigments* **2007**, *75*, 701.

39. Nesic, A. R.; Velickovicand, S. J.; Antonovi, D. G. *J. Hazard. Mater.* **2012**, *209-210*, 256.

40. Zhu, H. Y.; Jiang, R.; Fu, Y. Q.; Jiangand, J. H.; Xiao, L. *App. Surf. Sci.* **2011**, *258*, 1337.

41. Jiang, R.; Zhuand, H.; Fu, Y. *Env. Transport. Eng.* **2011**, *24*, 7565.

42. Tanhaei, B.; Ayati, A.; Bamoharram, F. F.; Lahtinenand, M.; Sillanpää, M. *J. Chem. Technol. Biotechnol.* **2015**, to appear.

43. Yao, W.; Shenand, C.; Lu, Y. *Compos. Sci. Technol.* **2013**, *87*, 8.

44. Cho, D. W.; Jeon, B. H.; Chon, C. M.; Schwartz, F. W.; Jeongand, Y.; Song, H. *J. Ind. Eng. Chem.* **2015**, *28*, 60.

45. Kou, T.; Wang, Y.; Zhang, C.; Sunand, J.; Zhang, Z. *Chem. Eng. J.* **2013**, *223*, 76.